PAPER

Check for updates

Constructing Ni–Co PBA derived 3D/1D/2D NiO/NiCo₂O₄/NiMn-LDH hierarchical heterostructures for ultrahigh rate capability in hybrid supercapacitors†

Dongyan Gao,‡[a] Renning Liu,‡[a] Dandan Han, [ID] *[a] Pengcheng Xu,[a] Ping Wang[a] and Yen Wei [ID] *[b]

Engineering hierarchical heterostructure materials has been recognised as a challenging but prepossessing strategy for developing hybrid supercapacitors. Thus, a Ni–Co PBA derived 3D/1D heterostructure NiO/NiCo₂O₄ based layered double hydroxide on carbon cloth (CC/NiO/NiCo₂O₄/NiMn-LDH) as a battery-type electrode was successfully designed *via* a controllable hydrothermal method. The 3D Ni–Co PBA nanocubes served as scaffolds, providing more space for the nickel-cobalt precursors to grow and then calcine to form a continuous conductive layer of 3D/1D CC/NiO/NiCo₂O₄. Subsequently, 2D ultrathin NiMn-LDH nanosheets were uniformly anchored on 3D/1D NiO/NiCo₂O₄, resulting in a unique hierarchical structure that effectively addressed the restacking issue and dead volume of NiMn-LDH, contributing to increased charge and electron transport rates, which promoted the reaction kinetics. Benefiting from abundant interfaces with the open channels of the nanoarchitecture, the CC/NiO/NiCo₂O₄/NiMn-LDH electrode showed an exceptional specific capacity of 1593.0 C g⁻¹ at 1 A g⁻¹ and a desirable rate performance of 92.9% at a current density of 8 A g⁻¹. Surprisingly, HSC devices can achieve an ideal specific energy of 44.28 W h kg⁻¹ at a specific power of 108.22 W kg⁻¹ with 97.59% cycling durability after 10 000 consecutive charge/discharge cycles. These remarkable properties indicate that the designed novel hierarchical heterostructure electrode has great potential for broad applications in electrochemical energy storage systems.

Introduction

Owing to the continuous evolution of industry and global energy shortages, there is an urgent need for sustainable energy supply and energy transformation strategies.[1–3] The development of a high-efficiency, sustainable, and promising energy storage and conversion system has become a research hotspot in recent years.[4–6] The hybrid supercapacitor (HSC) with a battery-type positive electrode and traditional capacitor-type negative electrode has emerged as a noteworthy and promising member of a large family of various green energy technologies by virtue of its exceptional specific power and fast charging-discharging capability.[7,8] Nevertheless, the specific power of HSCs is mainly determined by the morphologies, electrochemical activity and cycling stability of the electrode

materials.[9] To date, many novel materials have been investigated for energy storage devices due to their ultrahigh theoretical capacity and enriched reversible redox reactions, including metal oxides and metal hydroxides, which show favorable electrochemical performances when applied as an electrode.[10,11] Transition metal oxides (TMO) as anode candidates for various battery-type electrode materials have the advantages of low price, abundant reserves and a high theoretical capacity. Interestingly, metal–organic frameworks (MOF) have been used as templates in some studies to synthesize a metal oxide electrode material with tunable porosity and pore size and compositional advantages by annealing in air, which provides a wider diffusion channel and a higher specific surface area. In recent years, Prussian blue analogues (PBAs) have become an important class of MOF. Compared to ZIF-8 and MIL-88, PBAs are multifunctional precursors for the synthesis of many advanced electrode materials due to their diverse compositions, diverse shapes and uniform sizes. In particular, PBA-derived metal oxides can retain their porous properties and impart a richer structure to the material.[12] Ju *et al.* skillfully utilized polyvinyl pyrrolidone (PVP) in Mn-based PBA and annealed the material to form Mn₂O₃/Co₃O₄ composites, the specific capacity

[a]*College of Biology & Food Engineering, Jilin Institute of Chemical Technology, Jilin 132022, China. E-mail: luckhan2006@163.com*

[b]*Department of Chemistry and the Tsinghua Center for Frontier Polymer Research, Tsinghua University, Beijing, 100084, China. E-mail: weiyen@tsinghua.edu.cn*

† Electronic supplementary information (ESI) available. See DOI: https://doi.org/10.1039/d3ta00759f

‡ These authors contributed equally to this work.

of the electrode was 478.7 F g^{-1}.[13] Therefore, annealed PBA-derived metal oxides are considered to be electrode materials with unique design advantages and well controlled structures. However, due to poor electrical conductivity and the use of binders, the electrochemical properties of powdered electrodes are unsatisfactory, which may hinder their practical implementation. Bimetallic metal oxide ($NiCo_2O_4$) is prone to cause volume expansion in the continuous embedding and stripping of electrolyte ions, resulting in crushing and deterioration of the material, which reduces the specific capacitance and cycle stability of the material.[14] Zhang *et al.* prepared hierarchical $NiCo_2O_4$ microspheres self-assembled by nanorods, nanosheets and nanoparticles through hydrothermal and calcination processes, which exhibited a specific capacitance of 667.6 F g^{-1} at a current density of 1 A g^{-1}.[15] The self-supported electrode material could alleviate the volume change during charging and discharging, which can effectively improve the material's performance.

To overcome these problems and further improve performance, designing nanoarrays directly constructed on conductive substrates is a promising approach.[16] Although building independent arrays on the surface of conductive substrates is effective in improving their electrochemical properties, single-structure or single-component electrode materials still do not produce satisfactory results. Constructing multi-dimensional architectures combined with core–shell morphology is another important strategy to solve the problem and further improve electrochemical properties.[17] Layered double hydroxides (LDHs) are compounds with a unique 2D stacked arrangement of layers; in particular, nickel-manganese layered double hydroxides (NiMn-LDHs) have attracted extensive attention due to their highly interconnected morphology, flexible ion exchangeability and abundant active sites.[18–20] However, the low electron transfer efficiency of LDH during charge–discharge leads to poor rate characteristics. The construction of hierarchical electrode materials solves the problem of low conductivity of traditional LDH electrode materials. Increasing the interlayer spacing and reducing the particle size can also prevent the dense accumulation of LDH materials and structural performance degradation, as well as providing more reactive sites for the Faraday reaction. A lot of research has been carried out to improve the electrochemical activity of NiMn-LDHs and LDH-based electrodes.[21] For example, Liu *et al.* designed 1D $MgCo_2O_4$ nanowires to grow 2D NiMn-LDH nanosheets on nickel foam substrates by a simple hydrothermal and calcination method, producing a core–shell nanocomposite of $MgCo_2O_4$@NiMn-LDH/NF. The results show that the 3D $MgCo_2O_4$@NiMn-LDH/NF nanocomposite exhibits an excellent specific capacity of 3757.2 F g^{-1} at 1 A g^{-1} and a good rate capability (88.32%, 3318.4 F g^{-1} at 8 A g^{-1}) but capacity retention was only 86.9% after 6000 cycles.[22] Recently, Xiong and co-workers utilized the merits of 1D Co_3O_4, 2D $Ni(OH)_2$, and 3D Ni-M PBA (M = Co, Fe), exhibiting a superior electrochemical performance with a specific capacity of 643.6 C g^{-1} at 1 mA cm^{-2} with good rate capability, while the rate capability was 29% (at 220 mA cm^{-2}).[23] In conclusion, morphological size, surface area, porosity characteristics and

structure can control the accessibility, material diffusion and charge transport processes of active sites. Reducing any size to the nanoscale range will greatly increase the surface area, which in turn determines the number of electrochemically active sites.

Inspired by the above discussion, we synthesized 3D/1D/2D NiO/$NiCo_2O_4$/NiMn-LDH multidimensional structures, while 3D/1D NiO/$NiCo_2O_4$ was transformed from PBA on nickel foam with the hydrothermal method and calcination processes. The hybrid structure of 3D/1D/2D NiO/$NiCo_2O_4$/NiMn-LDH was constructed by growing two dimensional LDH nanosheets epitaxial on the NiO/$NiCo_2O_4$ surface. Meanwhile, the synthesis of NiO/$NiCo_2O_4$ nanocubes/nanowires based on the hydrothermal conversion of PBA is reported almost for the first time. Thanks to its special structure, the electrode exhibits an increased number of active sites and improved electrochemical ion transport kinetics, which makes the electrode achieve a higher specific capacity and an excellent long cycle performance. Moreover, as a hybrid supercapacitor, it obtains a higher specific energy density, lower resistance and good stability. This work provides a promising strategy for structural control engineering of multidimensional composite metal oxides/hydroxides to effectively promote their electrochemical performance.

Experimental section

Material preparation

Prior to synthesis, the pretreatment process of carbon cloth was as follows: carbon cloth (CC, 1 × 1 cm^2) was sequentially ultrasonically cleaned with 0.2 M HCl and 0.2 M HNO$_3$ for 30 min and rinsed with deionized (DI) water. DI water was used throughout the experiment. All the reagents were purchased from Aladdin and used without further purification.

Synthesis of the 3D CC/Ni–Co PBA nanocubes

CC/Ni–Co PBA was synthesized by a previously reported method.[24] An aqueous solution containing 0.6 mmol Ni(NO$_3$)$_2$ 6H$_2$O, 0.9 mmol Na$_3$C$_6$H$_5$O$_7$ 2H$_2$O and 20 mL DI water was rapidly added into another aqueous solution of 0.4 mmol K$_3$[Co(CN)$_6$] and 20 mL deionized (DI) water under continuous stirring. Two pieces of cleaned and weighed CC were placed in the above solution, which was reacted at 25 °C for 24 h. The samples were rinsed several times with DI water and then dried at 60 °C. The average loading mass of the CC/Ni–Co PBA nanocubes was about 0.1 mg cm^{-2}.

Synthesis of the 3D/1D CC/NiO/NiCo$_2$O$_4$ array architecture

The obtained CC/Ni–Co PBA was immersed in a solution containing 37.5 mL DI water, 1.0 mmol Co(NO$_3$)$_2$ 6H$_2$O, 0.5 mmol Ni(NO$_3$)$_2$ 6H$_2$O and 6.0 mmol CH$_4$N$_2$O. Then, the solution and CC/Ni–Co PBA were transferred into a 50 mL Teflon-line stainless steel autoclave and heated at 120 °C for 7 h. The substrate with the as-grown precursors was calcined at 350 °C in air atmosphere for 3 h with a heating rate of 2 °C min^{-1}. Finally, NiO/$NiCo_2O_4$ nanocubes/nanowires were obtained on CC with an average mass loading of 0.3 mg cm^{-2}.

This journal is © The Royal Society of Chemistry 2023

J. Mater. Chem. A, 2023, **11**, 9546–9554 | **9547**

Synthesis of the 3D/1D/2D CC/NiO/NiCo$_2$O$_4$/NiMn-LDH nanoarchitecture

The obtained CC/NiO/NiCo$_2$O$_4$ was immersed in a solution containing 40 mL DI water, 0.713 g NiCl$_2$ 6H$_2$O, 0.198 g MnCl$_2$ 4H$_2$O and 0.700 g HMT under continuous stirring for 15 min. The solution and CC/NiO/NiCo$_2$O$_4$ were transferred into a 50 mL Teflon-line stainless steel autoclave and heated at 90 °C for 2 h. Similarly, CC/NiO/NiCo$_2$O$_4$/NiMn-LDH-1, CC/NiO/NiCo$_2$O$_4$/NiMn-LDH-4 and CC/NiO/NiCo$_2$O$_4$/NiMn-LDH-6 were synthesized by a hydrothermal reaction for 1, 4, and 6 hours, respectively. Then, the substrate covered with CC/NiO/NiCo$_2$O$_4$/NiMn-LDH was taken out, washed with DI water and dried at 70 °C overnight in a vacuum drying oven. The mass loading of the CC/NiO/NiCo$_2$O$_4$/NiMn-LDH active materials was about 0.9 mg cm^{-2}. For comparison, the CC/NiMn-LDH was prepared without NiO/NiCo$_2$O$_4$ synthesis under the same conditions. The loading mass of CC/NiMn-LDH was about 0.7 mg cm^{-2}.

Characterization

The morphological analysis, crystal structure, and element valence information of the samples were characterized by SEM (SUPRA 40, German Zeiss), TEM (FEI, Tecnai G^2 F20), XRD (D/max TTR-III, Cu Kα) and XPS (FEI, Tecnai G^2 F20).

Using 2 M KOH alkaline solution as an electrolyte, all electrochemical tests of the as-prepared electrodes were recorded on a CHI660E electrochemical workstation with a three-electrode system. The CC (1 × 1 cm^2) supported as-prepared electrodes, saturated calomel electrode (SCE) and platinum foil were used as the working, reference and counter electrodes, respectively. The specific discharge capacity of the battery-type faradaic electrode materials was obtained from the GCD measurement by the following eqn (1):

$$C \ (\text{C g}^{-1}) = I \times \Delta t/m \tag{1}$$

where I (A) is the applied current, Δt (s) is the discharge time, m (g) is the mass of the active materials and C (C g^{-1}) is the specific discharge capacity. To achieve the superior electrochemical properties of the device, the load mass ratio between the positive and negative active materials was calculated by the charge conservation eqn (2):

$$m^+/m^- = C^- \times \Delta V^-/C^+ \times \Delta V^+ \tag{2}$$

where C^+ (C g^{-1}) and C^- (C g^{-1}) represent the specific discharge capacity of the electrode. ΔV^+ and ΔV^- represent the potential window of CC/NiO/NiCo$_2$O$_4$/NiMn-LDH and the AC electrodes, respectively. According to this equation, the active material mass loading of CC/AC was ∼7.0 mg cm^{-2}. The specific energy (E, W h kg^{-1}) and the specific power (P, W kg^{-1}) of the HSC devices were calculated using the following eqn (3) and (4):

$$E = I\int V(t)\mathrm{d}t/3.6M \tag{3}$$

$$P = 3600 \times E/\Delta t \tag{4}$$

where M (g), I (A), Δt (s) and $\int V(t)\mathrm{d}t$ represent the total mass of the positive and negative electrode active materials, the specific current, the discharge time of the HSC device, and $\int V(t)\mathrm{d}t$ is the area under the discharge curve, respectively.

Results and discussion

The 3D/1D/2D CC/NiO/NiCo$_2$O$_4$/NiMn-LDH heterostructures were successfully fabricated by a three-step process, as shown in Fig. 1. Firstly, 3D CC/Ni–Co PBA was used as the precursor by a typical precipitation method. It can be seen that the cubic Ni–Co PBA was uniformly distributed on the CC substrate, and the size is approximately 200 nm (Fig. 2a). Subsequently, CC/NiO/NiCo$_2$O$_4$ derived from 3D CC/Ni–Co PBA (Ni$_3$[Co(CN)$_6$]$_2$·12H$_2$O) nanocubes was obtained by further growth of nickel-cobalt precursors (nickel-cobalt hydroxide) followed by calcination. The reaction can be described in the following equations:[25]
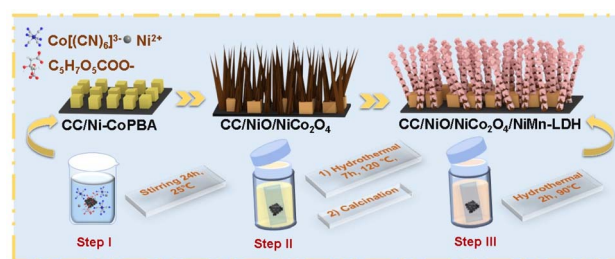

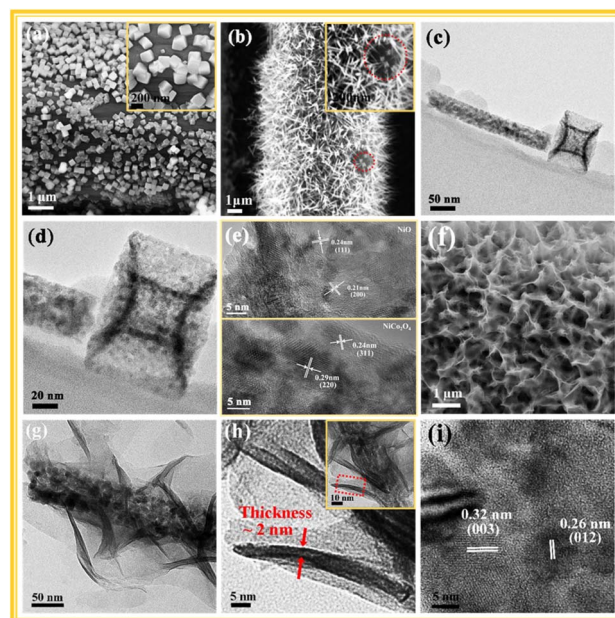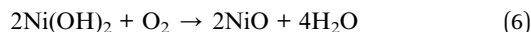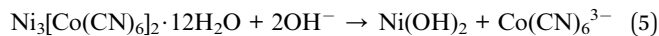**Fig. 1** A schematic illustration of the synthetic process of CC/NiO/NiCo$_2$O$_4$/NiMn-LDH.

Fig. 2 SEM images of (a) 3D Ni–Co PBA nanocubes and (b) 3D/1D NiO/NiCo$_2$O$_4$; (c, d) TEM images of 3D/1D NiO/NiCo$_2$O$_4$; (e) HRTEM images of 3D NiO and 1D NiCo$_2$O$_4$; SEM images of (f) the 3D/1D/2D NiO/NiCo$_2$O$_4$/NiMn-LDH hierarchical structure; (g) TEM image of the 3D/1D/2D NiO/NiCo$_2$O$_4$/NiMn-LDH; and (h, i) HRTEM images of the 3D/1D/2D NiO/NiCo$_2$O$_4$/NiMn-LDH.

9548 | *J. Mater. Chem. A*, 2023, **11**, 9546–9554

This journal is © The Royal Society of Chemistry 2023

$$Ni_3[Co(CN)_6]_2 \cdot 12H_2O + 2OH^- \rightarrow Ni(OH)_2 + Co(CN)_6^{3-} \quad (5)$$

$$2Ni(OH)_2 + O_2 \rightarrow 2NiO + 4H_2O \quad (6)$$

The SEM image in Fig. 2b reveals that CC/NiO/NiCo$_2$O$_4$ were synthesized by calcination on the carbon cloth substrate to form a large area of 3D/1D hybrid structure. The growth of the nanocubes does not completely cover the carbon cloth but leaves some "gaps". Some of the NiCo$_2$O$_4$ nanowires were formed in the "gap" between the nanocubes and the carbon cloth, rather than growing entirely on the nanocubes or the carbon cloth. The unique 3D/1D NiO/NiCo$_2$O$_4$ structure forms a self-supporting structure that facilitates electrolyte penetration and ion transport, allowing the two metal oxides to fully exhibit synergistic effects.[26] The as-prepared NiCo$_2$O$_4$ showed a porous nanowires structure and the NiCo$_2$O$_4$ porous nanowires' average diameter was approximately 30 nm (Fig. 2c and d). The HRTEM image of Fig. 2e shows that the lattice spacing is 0.29 nm and 0.24 nm, which could be indexed to the (220) and (311) planes of NiCo$_2$O$_4$. In addition, the morphology of 1D CC/NiCo$_2$O$_4$ is shown Fig. S1.† Subsequently, the 2D NiMn-LDH ultrathin nanosheets were epitaxially anchored to the 3D/1D CC/NiO/NiCo$_2$O$_4$ nanocubes/nanowires via a hydrothermal method to obtain a 3D/1D/2D CC/NiO/NiCo$_2$O$_4$/NiMn-LDH nanoarchitecture. As shown in Fig. 2f and g the NiMn-LDH nanosheets were uniformly and perfectly encapsulated in the NiO/NiCo$_2$O$_4$ surface to form a core–shell heterostructure with an increased number of active sites and an enhanced specific surface area. The HRTEM image of the NiO/NiCo$_2$O$_4$/NiMn-LDH composites clearly demonstrates the 2D ultrathin NiMn-LDH nanosheets with an average thickness of about 2 nm (Fig. 2h). Moreover, the HRTEM image (Fig. 2i) demonstrates that the lattice spacing measured from the lattice fringe is 0.32 nm and 0.26 nm corresponding well to the (003) and (012) planes of NiMn-LDH, which is in accordance with the XRD results. In Fig. S2,† the CC/NiMn-LDH nanosheets are uniformly loaded on the carbon cloth substrate. Interestingly, by changing the reaction time the morphologies of the 3D/1D/2D CC/NiO/NiCo$_2$O$_4$/NiMn-LDH can be easily adjusted. When the reaction time is insufficient (heating for 1 h), a slightly hierarchical structure can be obtained (Fig. S3†). By further extending the reaction time to 4 h or 6 h, CC/NiO/NiCo$_2$O$_4$/NiMn-LDH-4 and CC/NiO/NiCo$_2$O$_4$/NiMn-LDH-6 are completely covered by two-dimensional nanosheets and the 1D/2D/3D composite structure completely fails (Fig. S4 and S5†). One explanation for this phenomenon is that the size of the NiMn-LDH nanosheets increases with the reaction time.

The prepared sample was probed by using the XRD, XPS and elemental mapping images to explore the morphology and element distribution of the grown heterostructure. Fig. 3a shows the elemental mapping of the NiO/NiCo$_2$O$_4$/NiMn-LDH heterostructures and indicated that the Co, Ni, Mn and O elements are evenly distributed on the surface. Moreover, a core–shell structure was successfully synthesized from the narrowed Co distribution. The crystallographic structure and composition of the as-obtained samples were determined by
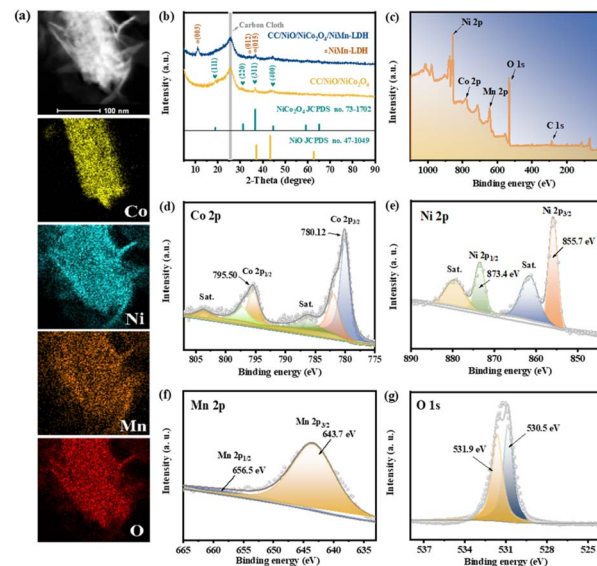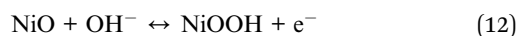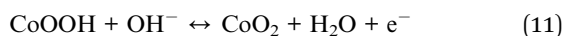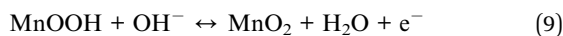

Fig. 3 (a) EDS mapping for Co, Ni, Mn and O elements of the NiO/NiCo$_2$O$_4$@NiMn-LDH. (b) The XRD pattern of CC/NiO/NiCo$_2$O$_4$/NiMn-LDH and CC/NiO/NiCo$_2$O$_4$. XPS spectra of (c) the survey spectrum, (d) Co 2p, (e) Ni 2p, (f) Mn 2p and (g) O 1s in the CC/NiO/NiCo$_2$O$_4$/NiMn-LDH.

XRD analysis. Additionally, the detailed XRD spectra of Ni–Co PBA before and after calcination are also shown in Fig. S6.† The XRD patterns confirm that Ni–Co PBA was successfully converted into NiO after annealing at 350 °C in air atmosphere for 3 h, its diffraction peaks are located at 37.25°, 43.28°, and 62.88°, which corresponds to the (111), (200) and (220) plane reflections of the NiO phase (JCPDS no. 47-1049), respectively.[25] Fig. 3b depicts the XRD patterns of CC/NiO/NiCo$_2$O$_4$ and CC/NiO/NiCo$_2$O$_4$/NiMn-LDH, respectively. As can be seen from the image, the CC substrate peak has obvious wide diffraction peaks at a 2θ value of 26.3°.[27] NiCo$_2$O$_4$ shows diffraction peaks which clearly correspond to the (111), (220), (311) and (400) standard planes (JCPDS 20-0781). The diffraction peaks of the (003), (012) and (015) planes are observed, which are justified according to previous literature on NiMn-LDH.[28] The co-existence of the four characteristic diffraction peaks indicated that CC/NiO/NiCo$_2$O$_4$/NiMn-LDH has been successfully fabricated. Moreover, the XRD patterns of CC/NiO/NiCo$_2$O$_4$/NiMn-LDH-1, CC/NiO/NiCo$_2$O$_4$/NiMn-LDH-4 and CC/NiO/NiCo$_2$O$_4$/NiMn-LDH-6 are displayed in Fig. S7.†

To further consider the surface chemical composition and element distribution of CC/NiO/NiCo$_2$O$_4$/NiMn-LDH, XPS measurements were conducted. The presence of Ni, Co, Mn, O and C elements in CC/NiO/NiCo$_2$O$_4$/NiMn-LDH is demonstrated by the survey spectrum (Fig. 3c). As characterized in the Co 2p spectrum (Fig. 3d), two spin orbit doublets peaks centered at 780.12 and 795.50 eV are accompanied by two shake-up satellites (identified as "Sat."), which are considered to be Co 2p$_{3/2}$ and Co 2p$_{1/2}$ respectively, which clearly indicates the existence of Co^{2+} and Co^{3+}.[29] Similarly, the Ni 2p spectrum (Fig. 3e) shows two peaks at 873.4 eV and 855.7 eV, which are characteristic of Ni^{2+}.[30–32] The Mn 2p$_{3/2}$ and Mn 2p$_{1/2}$ (Fig. 3f)

This journal is © The Royal Society of Chemistry 2023

J. Mater. Chem. A, 2023, 11, 9546–9554 | 9549

peaks are located at 643.7 and 656.5 eV, suggesting the presence of Mn^{3+} in the sample.[12,13,33] The O 1s XPS spectra (Fig. 3g) of CC/NiO/$NiCo_2O_4$/$NiMn$-LDH consist of three oxygen peaks, respectively. The O1 peak (530.5 eV) was associated with the typical metal oxygen bonds. The peak of O2 (531.9 eV) was ascribed to the hydroxyl groups, respectively.[34,35] XPS spectra of CC/NiO/$NiCo_2O_4$ is depicted in Fig. S8.† Specifically, the near surface of the prepared CC/NiO/$NiCo_2O_4$/$NiMn$-LDH has a mixed composition containing Ni^{2+}, Mn^{3+}, Co^{2+} and Co^{3+}, which is favorable for providing rich faradaic reaction sites. The related reaction equations are as follows:[13,24,36]

$$Ni(OH)_2 + OH^- \leftrightarrow NiOOH + H_2O + e^- \quad (7)$$

$$Mn(OH)_2 + OH^- \leftrightarrow MnOOH + H_2O + e^- \quad (8)$$

$$MnOOH + OH^- \leftrightarrow MnO_2 + H_2O + e^- \quad (9)$$

$$NiCo_2O_4 + OH^- + H_2O \leftrightarrow NiOOH + 2CoOOH + e^- \quad (10)$$

$$CoOOH + OH^- \leftrightarrow CoO_2 + H_2O + e^- \quad (11)$$

$$NiO + OH^- \leftrightarrow NiOOH + e^- \quad (12)$$

To confirm the applicability of CC/NiO/$NiCo_2O_4$/$NiMn$-LDH as an electrode for HSC devices, cyclic voltammetry (CV) and galvanostatic charge/discharge (GCD) tests were conducted in a standard three-electrode configuration with 2 M KOH aqueous solution as the electrolyte. As shown in Fig. 4a, the CV curves of CC/$NiCo_2O_4$ (see Fig. S9† for more details), CC/NiO/$NiCo_2O_4$ (Fig. S10†), CC/$NiMn$-LDH-2 (Fig. S11†), CC/NiO/$NiCo_2O_4$/$NiMn$-LDH-1, CC/NiO/$NiCo_2O_4$/$NiMn$-LDH-4 and CC/NiO/$NiCo_2O_4$/$NiMn$-LDH-6 (Fig. S12 and S13†) electrodes were conducted at a scan rate of 5 mV s^{-1} (−0.1 to 0.7 V). Clearly, a pair of redox peaks can be found from the CV curves, which can be attributed to the faradaic redox reactions of a battery-type faradaic material.[37] Apparently, the CC/NiO/$NiCo_2O_4$/$NiMn$-LDH heterostructure electrode demonstrates a larger enclosed CV curve area and higher peak current than the CC/$NiCo_2O_4$, CC/NiO/$NiCo_2O_4$ and CC/$NiMn$-LDH electrodes. This shows the superior performance of the abundant active sites to participate in faradaic redox reactions. Fig. 4b shows the GCD curves of all the electrodes at a specific current of 1 A g^{-1}, obviously, the CC/NiO/$NiCo_2O_4$/$NiMn$-LDH electrode delivers the longest discharge time than the other electrodes, and thus displays the highest charge-storage capacity. To determine the rate
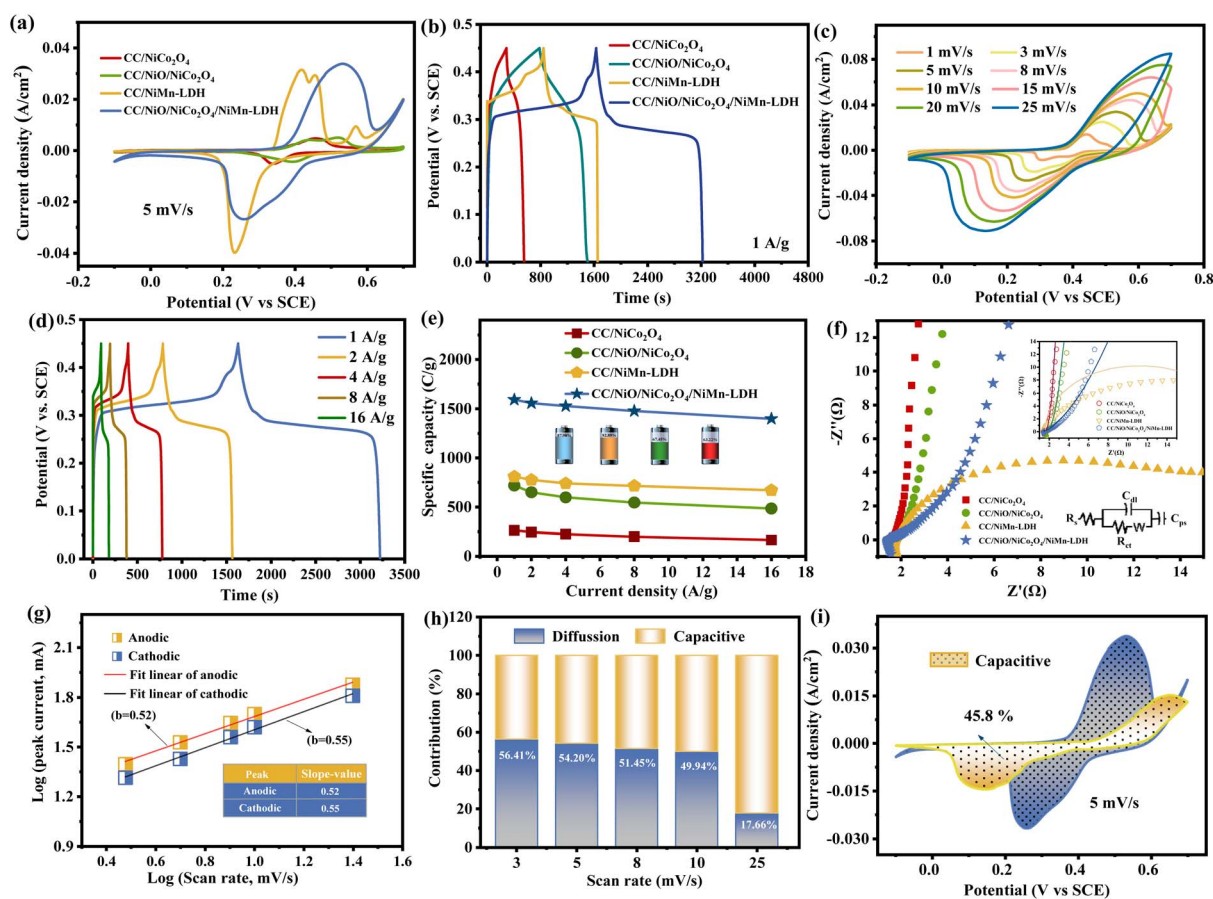

Fig. 4 Comparisons of CC/$NiCo_2O_4$, CC/NiO/$NiCo_2O_4$, CC/$NiMn$-LDH and CC/NiO/$NiCo_2O_4$/$NiMn$-LDH: (a) CV plots at 5 mV s^{-1}, (b) GCD plots at 1 A g^{-1}, (c) CV plots at a scan rate from 1 to 25 mV s^{-1} and (d) GCD plots at various specific currents for CC/NiO/$NiCo_2O_4$/$NiMn$-LDH, (e) capacity plots and (f) Nyquist plots, (g) slope values, (h) surface capacitive and diffusion contribution at various scan rates and (i) surface capacitive contribution (yellow region) at a scan rate of 5 mV s^{-1} for CC/NiO/$NiCo_2O_4$/$NiMn$-LDH.

9550 | *J. Mater. Chem. A*, 2023, **11**, 9546–9554

This journal is © The Royal Society of Chemistry 2023

capability of CC/NiO/NiCo$_2$O$_4$/NiMn-LDH, electrochemical tests were performed by measuring CV and GCD tests at different scan rates. Fig. 4c displays the CV curves with a pair of redox peaks of the CC/NiO/NiCo$_2$O$_4$/NiMn-LDH electrode at a scan rate of 1, 3, 5, 8, 10, 15, 20, and 25 mV s^{-1} in the potential range of −0.1 to 0.7 V. With the increasing scan rate, redox peaks further separate, as the anodic peak shifts toward a higher potential, whereas the cathodic peak shifts toward a lower potential due to the polarization of the electrode.[38] Notably, the shape of the curves changes insignificantly, which suggests that the electrode material is favourable for rapid redox reactions. Fig. 4d illustrates the GCD curves of CC/NiO/NiCo$_2$O$_4$/NiMn-LDH at current densities from 1 A g^{-1} to 16 A g^{-1}. Notably, an obvious voltage plateau is observed around 0.3–0.25 V, which evidently supports the CV results. In addition, the charging curve is almost symmetric to the discharging curve, indicating rapid and reversible redox reactions of the electrode.

Furthermore, the cycling stability of CC/NiO/NiCo$_2$O$_4$/NiMn-LDH in Fig. S14.† According to the equation, the specific capacity of the CC/NiO/NiCo$_2$O$_4$/NiMn-LDH electrode is calculated to be 1593.0, 1557.6, 1527.6, 1479.2 and 1401.6 C g^{-1} at current densities of 1, 2, 4, 8, and 16 A g^{-1}, respectively (Fig. 4e). Meanwhile, the CC/NiO/NiCo$_2$O$_4$/NiMn-LDH shows a remarkable rate capability (92.9% retention, even increasing the current density to 8 A g^{-1}) compared to other materials reported in the literature (Table 1). Apparently, the integrated collaborative structure can effectively enhance the accessible surface area for electrolyte penetration, thus greatly increasing the specific capacity and rate capability. Fig. 4f shows the electrochemical impedance spectroscopy (EIS) tests of the electrodes. It can be seen from the impedance spectrum that CC/NiO/NiCo$_2$O$_4$/NiMn-LDH showed a much lower internal/bulk resistance (R_s) and charge transfer resistance (R_{ct}). In addition, there is a higher linear slope in the low-frequency region, indicating the highly conductive nature of CC/NiO/NiCo$_2$O$_4$/NiMn-LDH compared to other electrodes. In addition, the fitted R_s, R_{ct} and Warburg impedance (W) values of each electrode are shown in Table S1.†

In order to deeply investigate the charge storage mechanism and reaction kinetics of the CC/NiO/NiCo$_2$O$_4$/NiMn-LDH electrode, CV curves were further analyzed (Fig. 4c). The relationship between the peak current (i) and scan rate (v) obeys the equation:[39]

$$i = av^b \quad (13)$$

where a and b can be used to explain the charge storage kinetics in the electrode, the b-value is the speed of reaction kinetics. The b-value varies between 0.5 and 1, depending on the ratio of diffusion-controlled ability and capacitive charge storage. $b = 0.5$ represents a diffusion-controlled charge storage mechanism and $b = 1.0$ indicates a capacitive charge storage mechanism.[40] Fig. 4g shows the b-values of the CC/NiO/NiCo$_2$O$_4$/NiMn-LDH electrode obtained by calculating the slope of $\log(i)$ vs. $\log(v)$ diagram, which are 0.52 and 0.55 (fitted from anodic peak and cathodic peak), respectively. This implies that the charge storage process of the CC/NiO/NiCo$_2$O$_4$/NiMn-LDH electrode is dominated by a diffusion-controlled battery-type behavior.[41] To further quantify the ratios of the diffusion contribution (k_1v) and capacitive contribution ($k_2v^{1/2}$), the following equation is employed.[42]

$$i(V) = k_1v + k_2v^{1/2} \quad (14)$$

where $i(V)$ refers to the peak current at a given potential, v is the scan rate, and both k_1 and k_2 are constants. The charge-storage contribution of the CC/NiO/NiCo$_2$O$_4$/NiMn-LDH electrode at diverse scan rates is shown in Fig. 4h. With the increase of scan rate, the contribution of the diffusion-controlled process gradually decreases, which is due to the limited diffusion of ions into bulk.[43] In this case, at a scan rate of 5 mV s^{-1}, the capacitive contribution (the yellow area) accounts for about 45.80% of the total capacity (Fig. 4i).

In summary, the excellent electrochemical performance of the core–shell heterostructure 3D/1D/2D CC/NiO/NiCo$_2$O$_4$/NiMn-LDH electrode, especially the remarkable rate capability, can be attributed to the following reasons: (a) the formation of materials such as NiO, NiCo$_2$O$_4$, and NiMn-LDH leads to an ingenious optimization of electrochemical performance by enabling multiple redox reactions and shortening the transfer path of the electrolyte ion by generating and using multiple electroactive sites. (b) The 3D/1D/2D NiO/NiCo$_2$O$_4$/NiMn-LDH core–shell heterostructure grown on the CC substrate facilitates the core and shell interface enriched electron transport efficiency, reduces the impedance, and promotes its structural durability during the electrochemical activity. (c) At the same time, the 1D nanowire array provided abundant empty space for

Table 1 A summary of the electrochemical performance of other reported materials in supercapacitors[a]

Electrode material	Electrolyte	C_s	Rate capability	Cycle stability of device	Ref
CC/CoNi-DH	1 M KOH	929.4 C g^{-1} (2 mA cm^{-2})	87.0% (30 mA cm^{-2})	81.5% (7500 cycles)	44
CC/NiCo$_2$O$_4$@NiMn-LDH	3 M KOH	466.3 C g^{-1} (1 mA cm^{-2})	59.8% (5 mA cm^{-2})	97.7% (10 000 cycles)	45
CC/NiCo$_2$O$_4$@NiMn-LDH	6 M KOH	752.8 C g^{-1} (1 A g^{-1})	90.0% (30 mA cm^{-2})	83.3% (2000 cycles)	46
CF/CuO@ZnCo–OH	6 M KOH	299.3 C g^{-1} (5 mA cm^{-2})	71.6% (30 mA cm^{-2})	91.7% (4000 cycles)	47
CC/NiCo$_2$O$_4$@NiFe-LDH	6 M KOH	189.6 C g^{-1} (1 mA cm^{-2})	18.3% (5 mA cm^{-2})	97.0% (5000 cycles)	48
NF/NiCoMoS@NiCoAl-LDH	3 M KOH	1336.0 C g^{-1} (1 A g^{-1})	80.6% (7 A g^{-1})	89.3% (10 000 cycles)	49
NF/NiCoSe$_2$@NiMn-LDH	6 M KOH	1446.1 C g^{-1} (2 A g^{-1})	83.6% (32 A g^{-1})	96.8% (10 000 cycles)	50
CC/Co$_3$O$_4$@NiCoLDH	1 M KOH	850 C g^{-1} (1 A g^{-1}) C g^{-1}	78.0% (20 A g^{-1})	87.6% (5000 cycles)	51
CC/NiO/NiCo$_2$O$_4$/NiMn-LDH	2 M KOH	1593.0 C g^{-1} (1 A g^{-1})	92.9% (8 A g^{-1})	97.59% (10 000 cycles)	This work

[a] CC: carbon cloth; CF: copper foam; NF: nickel foam.

growing 2D NiMn-LDH ultra-thin nanosheets to obtain a 3D/1D/2D hierarchical structure, which alleviates the volume change of the kinetic process of such a material and maintains its original shape.

To further investigate the application ability of the 3D/1D/2D CC/NiO/NiCo$_2$O$_4$/NiMn-LDH electrode in electrochemical energy storage devices, HSC was constructed by incorporating the 3D/1D/2D CC/NiO/NiCo$_2$O$_4$/NiMn-LDH as the positive electrode and active carbon (AC) as the negative electrode in 2 M KOH electrolyte (denoted as CC/NiO/NiCo$_2$O$_4$/NiMn-LDH//AC). The schematic in Fig. 5a also visibly shows the working mechanism of the HSC device during charging and discharging. During the charging process, the anions (OH$^-$) and cations (K$^+$) migrate to the oppositely charged CC/NiO/NiCo$_2$O$_4$/NiMn-LDH and CC/AC electrodes, respectively. The resulting oxidation reaction on the surface of the positive electrode initiates the charge separation of the negative electrode. Due to the 3D/1D/2D structure of the CC/NiO/NiCo$_2$O$_4$/NiMn-LDH electrode, more electrons and ions are accommodated on the electrode surface and oxidized/separated. During the discharge process, the oxidized/separated ions on the surface of the positive and negative electrodes are reduced and

separated back into the electrolyte. This moves electrons from the negative pole to the positive pole, causing the light bulb to light up. Fig. 5b depicts the CV curves of the CC/AC electrode on the negative potential side and the CC/NiO/NiCo$_2$O$_4$/NiMn-LDH electrode on the positive potential side was tested in a three-electrode system at a scan rate of 10 mV s^{-1} with the potential ranges of -0.1 to 0.7 and 0 to -1.0 V. These measurements demonstrated that the assembled HSC device can work up to 1.5 V at a scan rate of 5 mA cm^{-2} and 10 mV s^{-1} (Fig. 5c and S15†). Fig. 5d displays the CV curves of the HSC device at various scan rates from 10 to 50 mV s^{-1} at an operating voltage of 1.50 V. Even at high scan rates of 50 mV s^{-1}, the internal area of the CV curves increases and the shape of CV curves can maintain their outlines, revealing the remarkable reversibility and high stability of the HSC device. Simultaneously, the quasi-rectangular CV curve has a pronounced redox peak, illustrating the blended charge storage with a certain percentage of faradaic and capacitive contributions. GCD curves for the HSC device at a specific current of 1–5 mA cm^{-2} are shown in Fig. 5e, the Faraday charge-storage mechanism can be further illustrated in a non-linear charge/discharge curve. The discharge specific capacity of the HSC
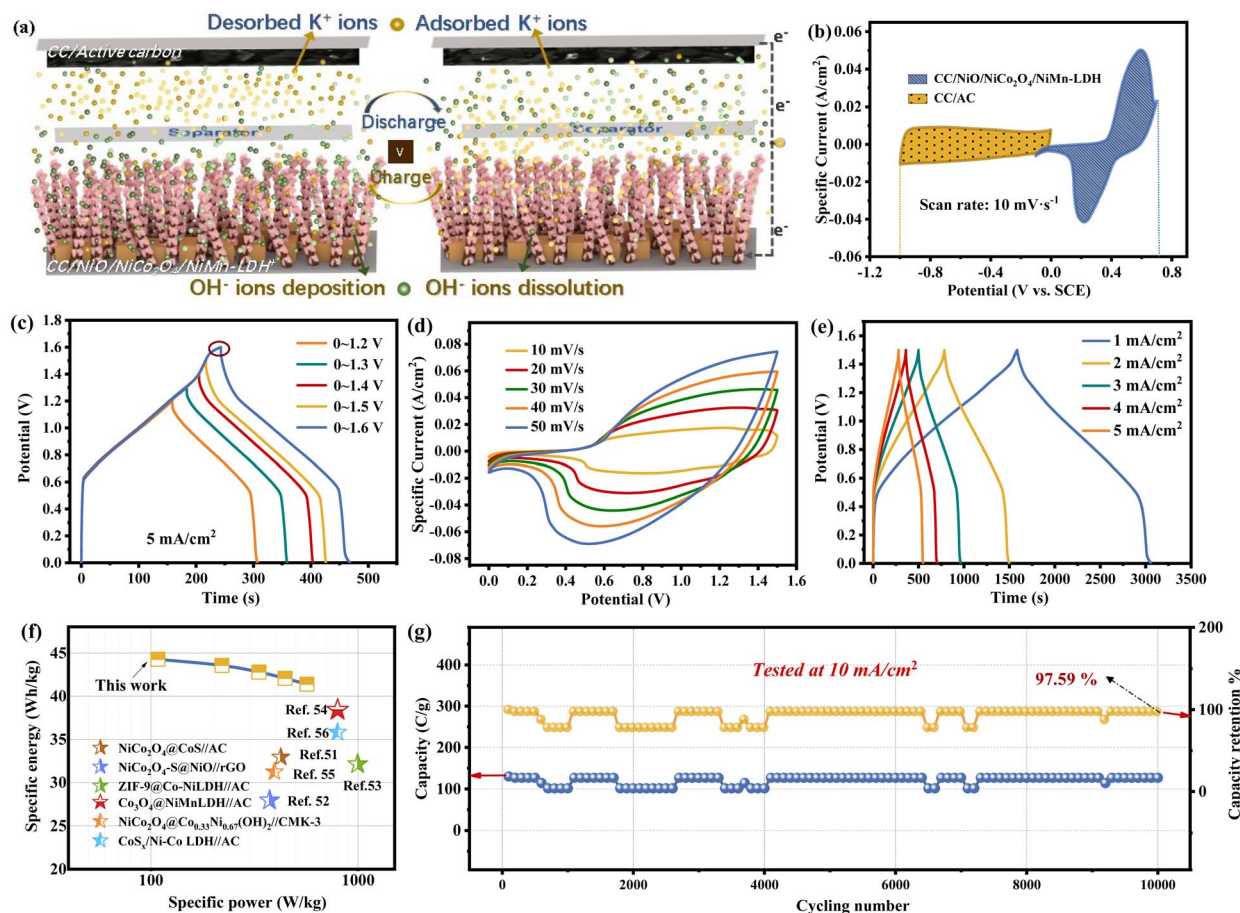

Fig. 5 (a) The charge−discharge mechanism and a schematic illustration of the HSC device. (b) CV plots of the CC/NiO/NiCo$_2$O$_4$/NiMn-LDH and CC/AC at 10 mV s^{-1} (c) GCD plots of the HSC device measured in various voltage windows at 5 mA cm^{-2}. (d) CV plots at the scan rate from 10 to 50 mV s^{-1}. (e) GCD plots at various specific currents and (f) a comparison of the Ragone plot of specific energy and specific power of HSC device. (g) Cycling stability of the HSC device at 10 mA cm^{-2}.

9552 | *J. Mater. Chem. A*, 2023, **11**, 9546–9554

This journal is © The Royal Society of Chemistry 2023

devices was studied by the GCD curve. The optimal capacity of the HSC device was 186.46 C g^{-1} at 1 mA cm^{-2}. Even at 5 mA cm^{-2}, a high specific discharge capacity was maintained at 90.94%, implying that the HSC device has a superior rate capability. The before and after cycling Nyquist curves of CC/NiO/NiCo$_2$O$_4$/NiMn-LDH//AC HSC are performed in Fig. S16.† Specific energy and specific power are two relevant performance indicators to evaluate the practical application and Ragone plots of the CC/NiO/NiCo$_2$O$_4$/NiMn-LDH//AC HSC device are displayed in Fig. 5f. The CC/NiO/NiCo$_2$O$_4$/NiMn-LDH//AC HSC achieves an ideal specific energy of 44.28 W h kg^{-1} at a specific power of 108.22 W kg^{-1}, while maintaining the specific energy of 41.38 W h kg^{-1} at a specific power of 556.12 W kg^{-1}. Furthermore, the CC/NiO/NiCo$_2$O$_4$/NiMn-LDH//AC HSC exhibited superior performance compared to recently reported devices such as NiCo$_2$O$_4$@CoS//AC,[52] NiCo$_2$O$_4$–S@NiO//rGO,[53] ZIF-9@CoAl LDHs//AC,[54] Co$_3$O$_4$@NiMn-LDH//AC,[55] NiCo$_2$O$_4$@Co$_x$Ni$_{1-x}$(OH)$_2$//CMK-3,[56] and CoS$_x$/Ni–Co LDH//AC.[57] The cycling stability of the HSC device was also tested by GCD curves and the specific discharge capacity is stable with 97.59% retention of 10 000 charge–discharge cycles at 10 mA cm^{-2} (Fig. 5g).

Conclusions

Here, 3D/1D NiO/NiCo$_2$O$_4$ is first synthesized *in situ* on carbon cloth *via* a simple hydrothermal method, which acts as a conductive skeleton that enables epitaxial growth of vertical NiMn-LDHs and increases the number of active sites. The as-prepared electrodes show an excellent electrochemical performance due to the 3D/1D/2D nanoarchitecture design of the composite by fine-tuning the reaction time and the contribution of the tight coordination between the different components. An exceptional specific capacity of 1593.0 C g^{-1} at a specific current of 1 A g^{-1} and a desirable rate performance of 92.9% (8 A g^{-1}) were obtained. Moreover, owing to the 3D/1D/2D nanoarchitecture with a rich redox process, the as-assembled CC/NiO/NiCo$_2$O$_4$/NiMn-LDH//AC HSC devices can achieve an ideal specific energy of 44.28 W h kg^{-1} at a specific power of 108.22 W kg^{-1} with 97.59% cycling durability. Hence, these excellent electrochemical performances make 3D/1D/2D CC/NiO/NiCo$_2$O$_4$/NiMn-LDH promising for practical applications.

Author contributions

Yen Wei and Dandan Han conceived and supervised the project. Dongyan Gao designed and performed the experiment. Renning Liu helped with the measurements of TEM, SEM and XRD. Pengcheng Xu evaluated the data and Ping Wang provided in-depth discussion. Dongyan Gao and Dandan Han wrote the manuscript. The manuscript was revised by all authors.

Conflicts of interest

The authors declare that they have no conflict of interest.

References

1 Y. Li, J. Zhang, Q. Chen, X. Xia and M. Chen, *Adv. Mater.*, 2021, **33**, 2100855.

2 W. Ma, W. Li, M. Li, Q. Mao, Z. Pan, J. Hu, X. Li, M. Zhu and Y. Zhang, *Adv. Funct. Mater.*, 2021, **31**, 2100195.

3 C. Ma, W. Cui, X. Liu, Y. Ding and Y. Wang, *InfoMat*, 2022, **4**, 12232.

4 M. Peng, L. Wang, L. Li, X. Tang, B. Huang, T. Hu, K. Yuan and Y. Chen, *Adv. Funct. Mater.*, 2022, **32**, 2109524.

5 Y. Ma, L. Zhang, Z. Yan, B. Cheng, J. Yu and T. Liu, *Adv. Energy Mater.*, 2022, **12**, 2103820.

6 K. Feng, Z. Sun, Y. Liu, F. Tao, J. Ma, H. Qian, R. Yu, K. Pan, G. Wang, S. Wei and Q. Zhang, *Nano Res.*, 2022, **15**, 6924.

7 G. Qu, P. Sun, G. Xiang, J. Yin, Q. Wei, C. Wang and X. Xu, *Appl. Mater. Today*, 2020, **20**, 100713.

8 L. Wan, L. Chen, M. Xie, J. Chen, Y. Zhang and C. Du, *J. Alloys Compd.*, 2022, **901**, 163567.

9 J. Sun, C. Wu, X. Sun, H. Hu, C. Zhi, L. Hou and C. Yuan, *J. Mater. Chem. A*, 2017, **5**, 9443–9464.

10 M. Wang, Y. Feng, Y. Zhang, S. Li, M. Wu, L. Xue, J. Zhao, W. Zhang, M. Ge, Y. Lai and J. Mi, *Appl. Surf. Sci.*, 2022, **596**, 153582.

11 L. Yang, X. He, Y. Wei, H. Bi, F. Wei, H. Li, C. Yuan and J. Qiu, *Nano Res.*, 2022, **15**, 4068–4075.

12 Y. Pang, L. Li, Y. Wang, X. Zhu, J. Ge, H. Tang, Y. Zheng, F. Wang, S. Wu, Q. Wu, Z. Shen and H. Chen, *Chem. Eng. J.*, 2022, **436**, 135202.

13 H. Ju, X. D. Liu, C. Y. Tao, F. Yang, X. L. Liu, X. Luo and L. Zhang, *J. Alloys Compd.*, 2021, **856**, 157134.

14 X. Sun, J. Sun, C. Wu, L. Guo, L. Hou and C. Yuan, *Mater. Today Energy*, 2021, **19**, 100592.

15 H. Zhang, J. Han, J. Xu, Y. Ling and X. Ou, *J. Mater. Sci.*, 2022, **57**, 5566–5567.

16 H. Xia, G. Li, H. Cai, X. Li, P. Sun, P. Wang, J. Huang, L. Wang, D. Zhang, Y. Yang and J. Xiong, *Dalton Trans.*, 2019, **48**, 12168–12176.

17 Y. Xuemin, L. Hejun, Y. Ruimei and L. Jinhua, *J. Mater. Sci. Technol.*, 2021, **62**, 60–69.

18 N. Zhao, Y. Feng, H. Zhao, H. Fan, S. Tian and B. Hu, *J. Alloys Compd.*, 2022, **901**, 163566.

19 C. Cheng, Y. Zou, F. Xu, C. Xiang, Q. Sui, J. Zhang, L. Sun and Z. Chen, *J. Energy Storage*, 2022, **52**, 105049.

This journal is © The Royal Society of Chemistry 2023

J. Mater. Chem. A, 2023, **11**, 9546–9554 | **9553**

20 K. Qu, M. Chen, W. Wang, S. Yang, S. Jing, S. Guo, J. Tian, H. Qi and Z. Huang, *J. Colloid Interface Sci.*, 2022, **616**, 584–594.

21 J. S. Gao, T. Lian, Z. Liu and Y. He, *J. Alloys Compd.*, 2022, **901**, 163558.

22 Z. Liu, A. Li, Y. Qiu, Q. Zhao, Y. Zhong, L. Cui, W. Yang, J. M. Razal, C. J. Barrow and J. Liu, *J. Colloid Interface Sci.*, 2021, **592**, 455–467.

23 D. Xiong, C. Lu, C. Chen, J. Wang, J. Chen, F. Y. Yi and X. Ma, *Mater. Chem. Front.*, 2021, **5**, 1388–1397.

24 J. Gao, Z. Liu, Y. Lin, Y. Tang, T. Lian and Y. He, *Chem. Eng. J.*, 2020, **388**, 124368.

25 Z. Peng, W. Wang, H. Zhao, J. Qi, H. Zhang, C. Zhou, B. Yan and Z. Zhang, *J. Electrochem. Soc.*, 2021, **168**, 080542.

26 F. Yang, K. Zhang, W. Li and K. Xu, *J. Colloid Interface Sci.*, 2019, **556**, 386–391.

27 W. Song, B. Wang, X. Cao, Q. Chen and Z. Han, *Inorg. Chem. Front.*, 2021, **8**, 5100–5112.

28 L. Wang, Y. Yang, B. Wang, C. Duan, J. Li, L. Zheng, J. Li and Z. Yin, *J. Alloys Compd.*, 2021, **885**, 160899.

29 R. BoopathiRaja and M. Parthibavarman, *Electrochim. Acta*, 2020, **346**, 136270.

30 X. Chen, S. Wang, G. Qiao, G. Lu, H. Cui and X. Wang, *Energy Fuels*, 2020, **34**, 16783–16790.

31 J. Zhao, J. Chen, S. Xu, M. Shao, Q. Zhang, F. Wei, J. Ma, M. Wei, D. G. Evans and X. Duan, *Adv. Funct. Mater.*, 2014, **24**, 2938–2946.

32 Y. Shang, S. Ma, Y. Wei, H. Yang and Z. Xu, *Ionics*, 2020, **26**, 3609–3619.

33 H. Liang, J. Lin, H. Jia, S. Chen, J. Qi, J. Cao, T. Lin, W. Fei and J. Feng, *J. Mater. Chem. A*, 2018, **6**, 15040–15046.

34 X. Guo, T. Zheng, G. Ji, N. Hu, C. Xu and Y. Zhang, *J. Mater. Chem. A*, 2018, **6**, 10243–10252.

35 Y. Wang, W. Li, L. Zhang, X. Zhang, B. Tan, J. Hao, Z. Jian, X. Wang, Q. Hu and X. Lu, *J. Power Sources*, 2020, **449**, 227487.

36 N. R. Chodankar, D. P. Dubal, S. H. Ji and D. H. Kim, *Small*, 2019, **15**, 1901145.

37 K. Song, W. Li, J. Xin, Y. Zheng, X. Chen, R. Yang, W. Lv and Q. Li, *Chem. Eng. J.*, 2021, **419**, 129435.

38 Y. Pan, J. Wei, D. Han, Q. Xu, D. Gao, Y. Yang and Y. Wei, *Inorg. Chem. Front.*, 2021, **8**, 4676–4684.

39 L. Wan, D. Chen, J. Liu, Y. Zhang, J. Chen, M. Xie and C. Du, *J. Power Sources*, 2020, **465**, 228293.

40 H. Che, Y. Lv, A. Liu, H. Li, Z. Guo, J. Mu, Y. Wang and X. Zhang, *Chem. Eng. J.*, 2020, **384**, 123372.

41 Q. Zong, H. Yang, Q. Wang, Q. Zhang, Y. Zhu, H. Wang and Q. Shen, *Chem. Eng. J.*, 2019, **361**, 1–11.

42 Y. Wang, H. Wei, H. Lv, Z. Chen, J. Zhang, X. Yan, L. Lee, Z. M. Wang and Y. L. Chueh, *ACS Nano*, 2019, **13**, 11235–11248.

43 Z. Yuan, H. Wang, J. Shen, P. Ye, J. Ning, Y. Zhong and Y. Hu, *J. Mater. Chem. A*, 2020, **8**, 22163–22174.

44 Y. Wu, H. Chen, Y. Lu, J. Yang, X. Zhu, Y. Zheng, G. Lou, Y. Wu, Q. Wu, Z. Shen and Z. Pan, *J. Colloid Interface Sci.*, 2021, **581**, 455–464.

45 H. Xiao, Y. Ma, M. Xu, R. Liu, X. Li, X. Wang, Y. Wang, Y. Liu and G. Yuan, *J. Colloid Interface Sci.*, 2022, **611**, 149–160.

46 S. Li, Y. Luo, C. Wang, M. Wu, Y. Xue, J. Yang and L. Li, *J. Colloid Interface Sci.*, 2022, **920**, 165986.

47 G. Liu, X.-Z. Song, S. Zhang, X. Chen, S. Liu, Y. Meng and Z. Tan, *J. Power Sources*, 2020, **465**, 228239.

48 D. Luo, Y. Yong, J. Hou, W. Guo, H. Liu, X. Zhao, J. Xiang, N. Zong, Y. Han and M. Yan, *ChemNanoMat*, 2022, **8**, 202200137.

49 K. Zhang, H. Zeng, M. Wang, H. Li, W. Yan, H. Wang and Z. Tang, *J. Mater. Chem. A*, 2022, **10**, 11213–11224.

50 B. Ameri, A. M. Zardkhoshoui and S. S. Hosseiny Davarani, *Sustain. Energy Fuels*, 2020, **4**, 5144–5155.

51 Y. Xuemin, L. Hejun, Y. Ruimei and L. Jinhua, *J. Mater. Sci. Technol.*, 2021, **62**, 60–69.

52 W. D. Wang, X. F. Li, P. P. Zhang, B. Q. Wang, S. H. Gong, X. C. Wang, F. Liu and J. P. Cheng, *J. Electroanal. Chem.*, 2021, **891**, 115257.

53 Y. Ouyang, R. Huang, X. Xia, H. Ye, X. Jiao, L. Wang, W. Lei and Q. Hao, *Chem. Eng. J.*, 2019, **355**, 416–427.

54 G. Wang, Y. Li and Z. Jin, *New J. Chem.*, 2020, **44**, 7528–7540.

55 W. Quan, Y. Xu, Y. Wang, S. Meng, D. Jiang and M. Chen, *Appl. Surf. Sci.*, 2019, **488**, 639–647.

56 K. Xu, R. Zou, W. Li, Q. Liu, X. Liu, L. An and J. Hu, *J. Mater. Chem. A*, 2014, **2**, 10090–10097.

57 X. Guan, M. Huang, L. Yang, G. Wang and X. Guan, *Chem. Eng. J.*, 2019, **372**, 151–162.

9554 | *J. Mater. Chem. A*, 2023, **11**, 9546–9554

This journal is © The Royal Society of Chemistry 2023